EXTENDED DATA

A novel PLpro inhibitor scaffold that protects mice from Long-COVID

Stefanie M. Bader[1,2,10], Dale J. Calleja[1,2,10], Shane M. Devine[1,2,10,#], Nathan W. Kuchel[1,10], Bernadine G. C. Lu[1,2], Xinyu Wu[1,2], Richard W. Birkinshaw[1,2], Reet Bhandari[1,2], Katie Loi[1,2], Rohan Volpe[1,2], Yelena Khakham[1], Amanda E. Au[1,2], Timothy R. Blackmore[1,2], Liana Mackiewicz[1], Merle Dayton[1], Jan Schaefer[1,2], Lena Scherer[1], Angus T. Stock[1,2], James P. Cooney[1,2], Kael Schoffer[1,2], Ana Maluenda[1], Elizabeth A. Kleeman[1,3], Kathryn C. Davidson[1,2], Cody C. Allison[1,2], Gregor Ebert[1,2], Gong Chen[4], Theresa A. Klemm[1,2], Ueli Nachbur[1,2], Smitha Rose Georgy[5], Peter E. Czabotar[1,2], Anthony J. Hannan[3,6], Tracy L. Putoczki[1,2,7], Maria Tanzer[1,2], Marc Pellegrini[1,2,9], Bernhard C. Lechtenberg[1,2], Susan A. Charman[4], Melissa J. Call[1,2], Jeffrey P. Mitchell[1,2], Kym N. Lowes[1,2], Guillaume Lessene[1,2,8,#], Marcel Doerflinger[1,2,#], David Komander[1,2,#]

[1] Walter and Eliza Hall Institute of Medical Research, Parkville, Victoria, Australia.

[2] Department of Medical Biology, University of Melbourne, Melbourne, Australia.

[3] Florey Institute of Neuroscience and Mental Health, University of Melbourne, Parkville, Victoria, Australia.

[4] Centre for Drug Candidate Optimisation, Monash Institute of Pharmaceutical Sciences, Monash University, Parkville, Victoria, Australia

[5] Anatomic Pathology – Veterinary Biosciences, Melbourne Veterinary School, University of Melbourne, Werribee, Victoria, Australia

[6] Department of Anatomy and Physiology, University of Melbourne, Parkville, Victoria, Australia.

[7] Department of Surgery, University of Melbourne, Melbourne, Australia

[8] Department of Biochemistry and Pharmacology, University of Melbourne, Melbourne, Australia

Current address: [9] Centenary Institute of Cancer Medicine and Cell Biology, Camperdown, NSW, Australia

[10] These authors contributed equally.

[#] Corresponding authors. David Komander, dk@wehi.edu.au; Marcel Doerflinger, doerflinger.m@wehi.edu.au; Guillaume Lessene, glessene@wehi.edu.au; Shane M Devine, devine.s@wehi.edu.au.

EXTENDED DATA FIGURE 1

a

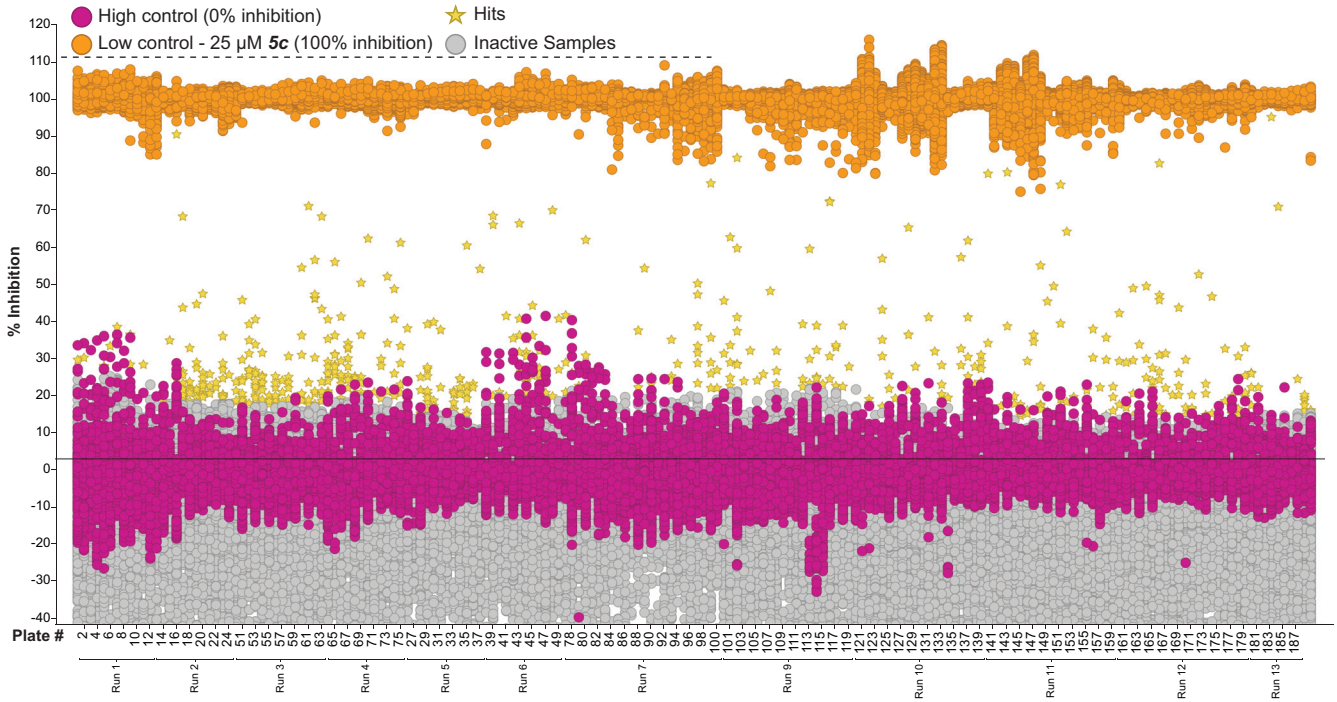

b

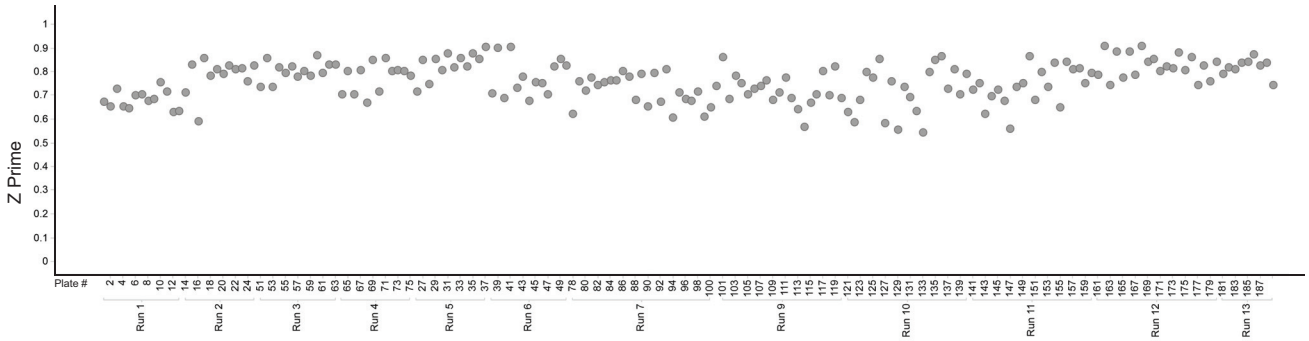

c

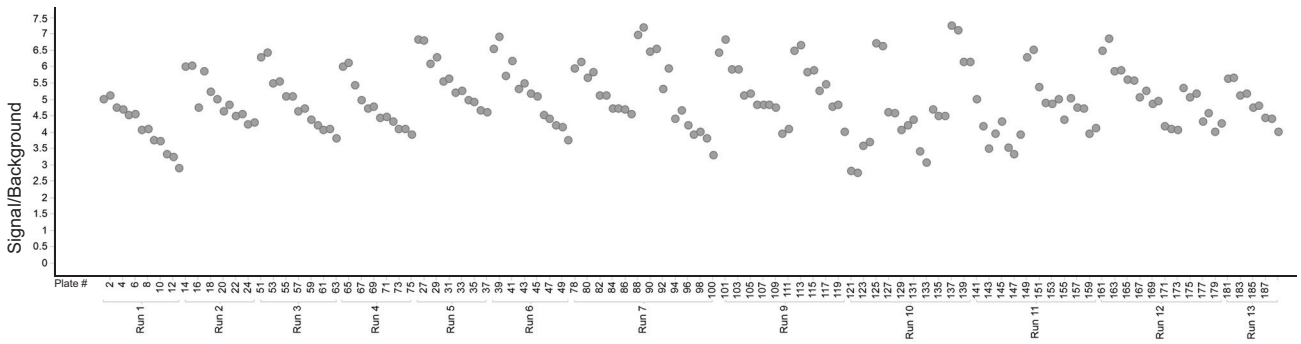

Extended Data Figure 1. High Throughput Screen of SARS-CoV-2 PLpro
Representative results from the primary screen by plate number grouped by run number (#). The UbRh assay (see **Fig. 1a**) assay was used to identify inhibitors of PLpro (see **Methods**). **(a)** A total of 412,644 compounds were screened at a single concentration. Hits were identified based on the criteria that they were 3 standard deviations above the mean of the high control (0% inhibition). **(b)** Representative Z Prime (Z') analysis of the primary screen by plate number. All plates met quality criteria of Z' > 0.5. **(c)** Representative signal/background (S/B) analysis of the primary screen by plate number. All plates met the quality control criteria (S/B > 3).

EXTENDED DATA FIGURE 2

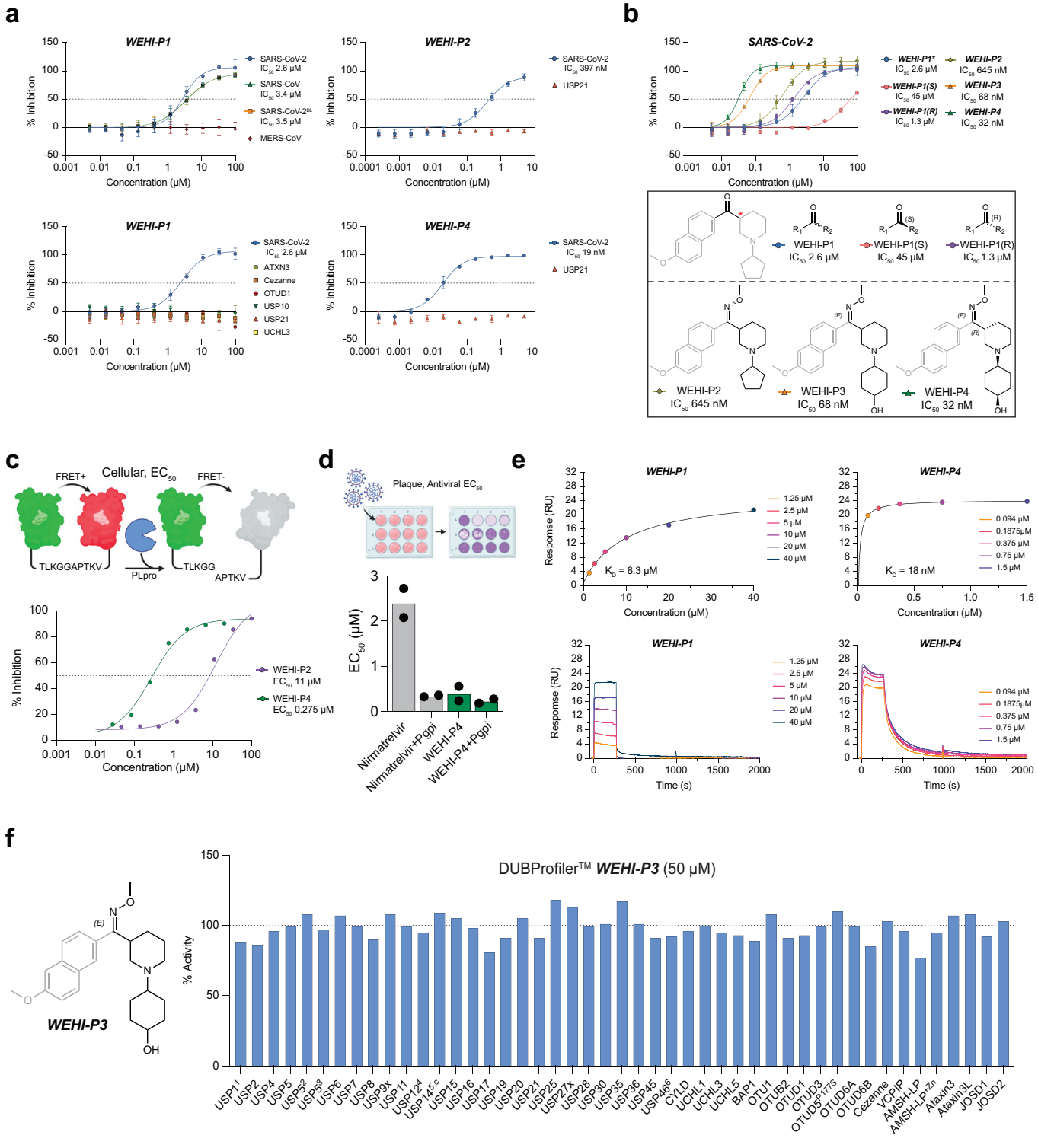

Extended Data Figure 2. Assay pipeline to assess compound activity of the *WEHI-P* series.

(a-b) The Ubiquitin Rhodamine110 assay (see **Fig. 1a**) was used to assess the activity of all compounds against all PLpro variants and control DUBs. Biochemical IC_{50} is displayed as the mean ± SD of n = 2-4 independent experiments each with technical duplicates. A representative curve for each is shown. ***WEHI-P1*** upper panel, n=3 for SARS-CoV-2, n=4 for SARS-CoV and n=2 for the remaining DUBs; ***WEHI-P1*** lower panel, n=4 for all PLpro variants; ***WEHI-P2***, n=4 and ***WEHI-P4***, n=2. See **Methods** for further assay details. **(b)** The UbRh assay was used to assess the activity of ***WEHI-P1*** and its enantiomeric pairs ***WEHI-P1(S)*** and ***WEHI-P1(R)***, ***WEHI-P2***, ***WEHI-P3*** and ***WEHI-P4***. **(c)** Cellular FRET biosensor assay used for measuring in cell activity of PLpro inhibitors, as reported in [27]. The mClover3 (green)/mRuby3 (red) FRET pair are joined by an amino acid sequence corresponding to the Nsp2-3 cleavage site found in SARS-CoV-2. Cleavage of this sequence by PLpro releases the FRET pair and induces a loss in fluorescent signal. ***WEHI-P1*** exhibited low activity in this assay (>20 μM, data not shown). Data is displayed as the mean of two independent experiments (n=2) performed with technical triplicate in each experiment. experiments performed in duplicate. **(d)** An antiviral plaque assay was used to assess the activity of ***WEHI-P*** series on viral replication. ***WEHI-P1*** to ***WEHI-P3*** showed low activity (>5 μM, data not shown). Nirmatrelvir was used to benchmark ***WEHI-P4*** with or without the Pgp inhibitor CP100356 (2 μM, labelled Pgpi). Data is displayed as the mean of experiments performed in duplicate. **(e)** SPR was used to measure direct binding of compound from the ***WEHI-P*** series to PLpro. *Top*, fitted binding curve; *bottom*, raw sensorgram data. K_D shown is the mean of experiments performed in technical duplicate. Representative graphs are shown. **(f)** Inhibitor ***WEHI-P3*** was tested at the DUBprofiler platform at Ubiquigent (Dundee, UK) assessing inhibitory potential against humans DUBs at 50 μM inhibitor concentration. USP1[1], USP1 assay performed in the presence of UAF1; USP5[2], USP5 assay performed with addition of ubiquitin at K_D; USP5[3], USP5 assay performed with addition of ubiquitin at B_{max}; USP12[4] indicates USP12 in the presence of modulating enzymes UAF1/WDR20; USP14[5] indicates assay performed in the presence of proteasome-vinyl sulfone at K_D; USP14[c] indicates the proteasome-vinyl sulfone control showed no activity in the absence of USP14; USP46[6], indicates USP46 in the presence of UAF1/WDR20.

EXTENDED DATA FIGURE 3

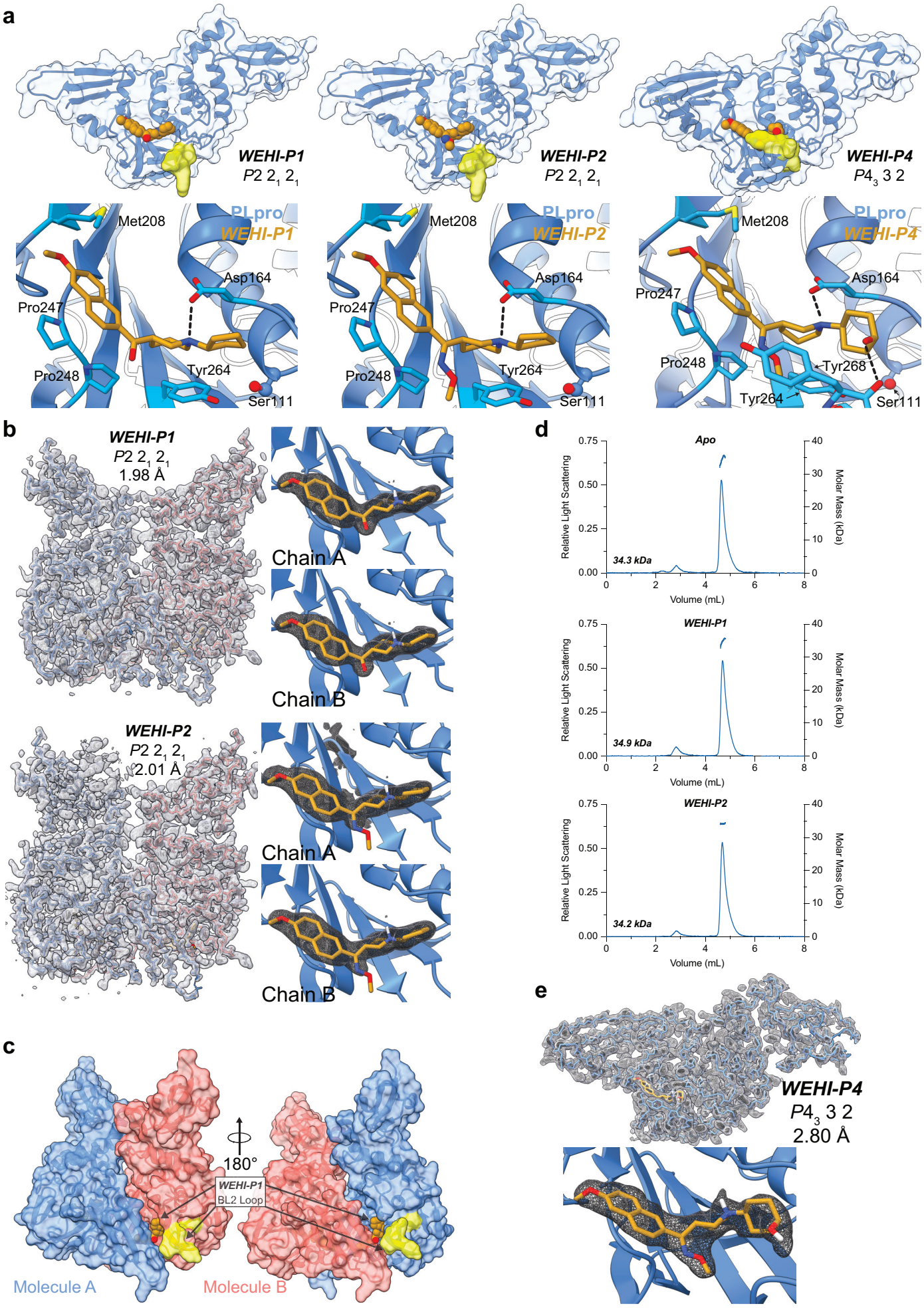

Extended Data Figure 3. Structural insights of the WEHI-P series.
(a) Crystal structure of SARS-CoV-2 PLpro in complex with ***WEHI-P1***, ***WEHI-P2*** and ***WEHI-P4*** were solved in two different space groups. The BL2 region of PLpro is coloured yellow. In ***WEHI-P1*** and ***WEHI-P2*** complex structures in space group $P2\ 2_1\ 2_1$, the BL2 loop does not contribute to compound binding but is involved in a crystal contact. In ***WEHI-P4*** the BL2 region is in the 'closed' conformation to contact the compound. A zoomed view of PLpro bound to each compound is also shown below. **(b)** 2|Fo| – |Fc| electron density contoured at 1 σ of the contents of the asymmetric unit. Insets show the compound binding sites with ligand density. For ***WEHI-P2***, the oxime group remained unresolved. **(c)** Surface representation of the protein chains in asymmetric unit of the $P2\ 2_1\ 2_1$ crystal setting (***WEHI-P1***, ***-P2***). Compounds were wedged between molecules. For this reason, we determined compound structures in another space group. **(d)** SEC–MALS analysis of SARS-CoV-2 PLpro apo form or in the presence of 100 μM ***WEHI-P1*** or ***WEHI-P2***. Absorbance was measured at a wavelength of 280 nm. Relative light scattering (Rayleigh Ratio) and calculated molecular mass over each peak is shown, with the observed molecular weights indicated in the bottom left. SEC–MALS experiments were performed once each with $PLpro^{WT}$ and $PLpro^{C111S}$, which displayed identical behaviour (graphs for $PLpro^{WT}$ are shown). **(e)** 2|Fo| – |Fc| electron density map at 1 σ, of the asymmetric content of the ***WEHI-P4*** complex in space group $P4_3\ 3\ 2$, with an overall view (top) and showing the ligand density (below). In this structure, the oxime is resolved clearly, and there are no crystal contacts affecting the compound binding site.

EXTENDED DATA FIGURE 4

a

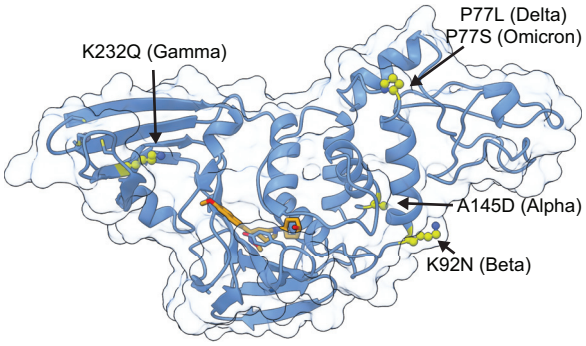

b

% Identity	SARS-CoV-2	SARS-CoV	MERS-CoV	HKU1	OC43	NL63	229E
SARS-CoV-2	100	83	30	28	28	20	19
SARS-CoV	83	100	31	28	29	20	21
MERS-CoV	30	31	100	29	28	20	21
HKU1	28	28	29	100	61	17	21
OC43	28	29	28	61	100	19	19
NL63	20	20	20	17	19	100	50
229E	19	21	21	21	19	50	100

100%
0%

c

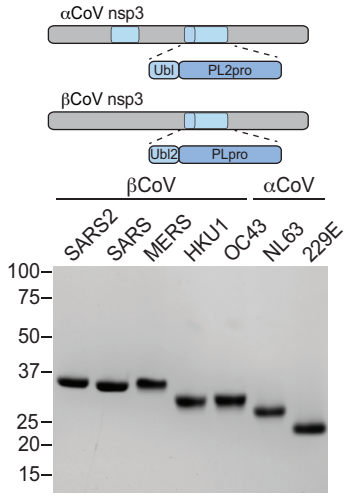

d

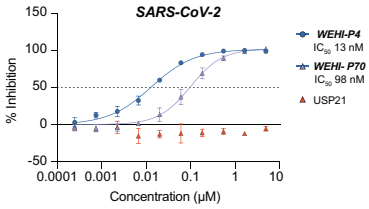

e

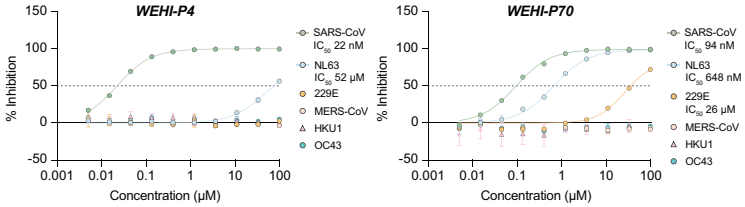

f

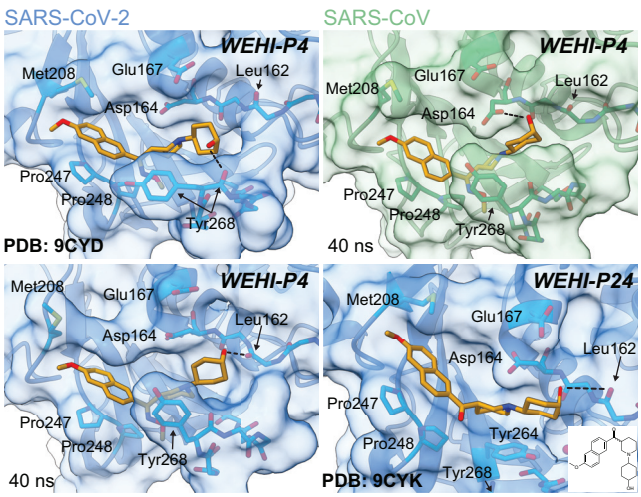

g

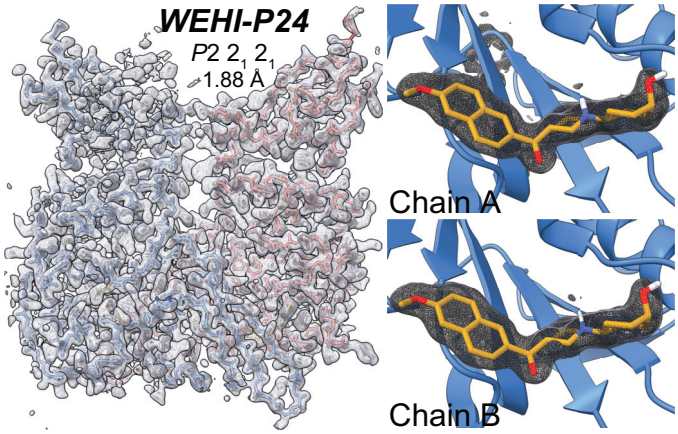

Extended Data Figure 4. Molecular Insights into pan-CoV activity of *WEHI-P70.* **(a)** SARS-CoV-2 PLpro bound to ***WEHI-P4*** (**Fig. 1c**), highlighting mutations from currently circulating SARS-CoV-2 variants of concern. All mutations are remote from compound binding sites. **(b)** Sequence identity matrix of the PLpro and PL2pro domains from the seven human transmissible coronaviruses, see sequence alignment in **Extended Data Fig 5**. **(c)** PLpro (βCoVs) and PL2pro (αCoVs) domains were expressed and purified to homogeneity for use in UbRh biochemical activity assays, against ***WEHI-P*** series compounds (see **Methods** for constructs). **(d-e)** Biochemical IC_{50} is displayed as the mean of n = 2 independent experiments each with technical duplicates. A representative curve for each is shown. See **Methods** for further assay details **(d)** Biochemical IC_{50} comparing ***WEHI-P4*** and ***WEHI-P70*** in inhibiting SARS-CoV-2 PLpro. Both compounds remain selective over USP21. USP21 data for ***WEHI-P70*** is shown (see Extended Data Figure 2a for ***WEHI-P4***). **(e)** Biochemical IC_{50}s comparing ***WEHI-P4*** and ***WEHI-P70*** in inhibiting PLpro from different CoVs. **(f)** Comparison of experimental structures of ***WEHI-P4*** and ***WEHI-P24*** bound to SARS-CoV-2 PLpro with 40 ns molecular dynamics simulations of docking ***WEHI-P4*** into SARS-CoV-2 and SARS-CoV PLpro. Key residues are noted. The cyclohexanol forms a H-bond with either the backbone of Leu162 or with that of Tyr268. **(g)** A further compound structure of PLpro bound to ***WEHI-P24*** was determined at 1.88 Å resolution in $P2\ 2_1\ 2_1$ (see **Extended Data Table 1**). 2|Fo| – |Fc| electron density at 1 σ covers the protein chains (*left*) and ligand binding site (*right*).

EXTENDED DATA FIGURE 5

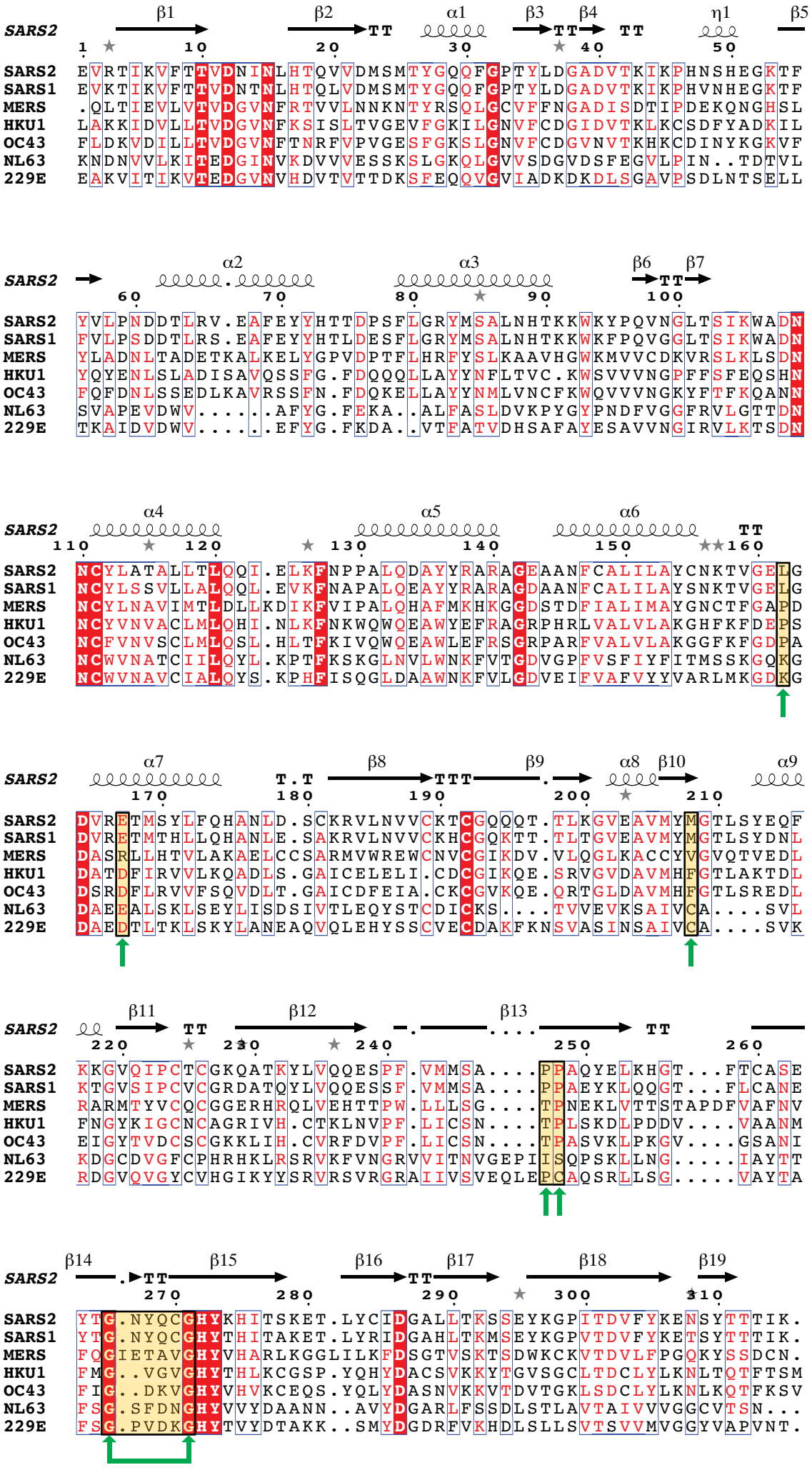

Extended Data Figure 5. Multiple Sequence Alignment of PLpro domains. Sequence alignment of the PLpro domains from the seven human transmissible coronaviruses. For αCoVs 229E and NL63, the PL2pro domain is evolutionarily related and serves a DUB domain[31] . Key residues found in the inhibitor binding sites for ***WEHI-P*** series compounds are highlighted and indicated with green arrows.

EXTENDED DATA FIGURE 6

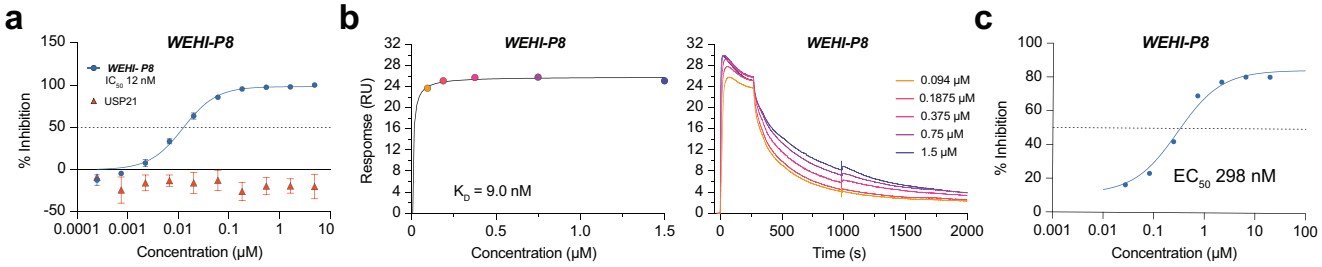

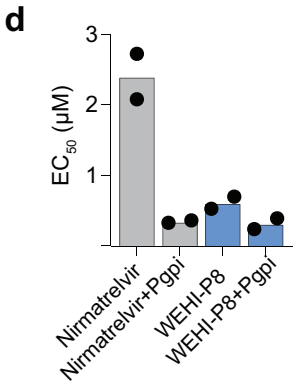

e

***In vitro* PK**	***WEHI-P8***
Mouse microsomes	$t_{1/2}$ = 41 .5 min CL_{int} = 33.4 μL/min/mg protein
Human microsomes	$t_{1/2}$ = 144 min CL_{int} = 9.7 μL/min/mg protein
Mouse hepatocytes	$t_{1/2}$ = 82.6 min CL_{int} = 16.8 μL/min/10^6 cells
Human hepatocytes	$t_{1/2}$ = 139 min CL_{int} = 10.0 μL/min/10^6 cells
Kinetic solubility (pH 2.0 / 6.5)	>320 / 160-320 μM
gLogD (pH 7.4)	3.8
m/h PPB	93.8 / 84.7 %
hERG	IC_{50} = 5.39 μM
CYP450 (7 isoforms)	IC_{50} > 10 μM

Extended Data Figure 6. Properties of *WEHI-P8.*

(a) Biochemical IC_{50} of ***WEHI-P8*** is displayed as the mean of n = 2 independent experiments each with technical duplicates. A representative curve is shown. See **Methods** for further assay details **(b)** Cellular FRET assay (cellular EC_{50}) of ***WEHI-P8***. Data is displayed as the mean from two independent experiments (n=2) each with technical triplicates. **(c)** SPR binding assay (K_D) of ***WEHI-P8.*** Values for SPR indicate the mean of n = 2 experiments and a representative graph is shown. **(d)** Antiviral plaque assay to assess activity of ***WEHI-P8*** on viral replication. Nirmatrelvir was used to benchmark ***WEHI-P8*** with or without the Pgp inhibitor CP100356 (2 μM, labelled Pgpi). Data is displayed as the mean of experiments performed in duplicate. Pgp inhibition is not required for ***WEHI-P8***. **(e)** DMPK properties for ***WEHI-P8***. CL_{int} , Intrinsic clearance; gLogD, partition co-efficient estimation using a gradient chromatography method; m/h PPB, mouse/human protein plasma binding; hERG, human ether-à-go-go-related gene; CYP450, cytochrome P450. ***WEHI-P8*** showed moderate stability in mouse microsomes ($T_{1/2}$ = 41.5 min, CL_{int} = 33.4 μL/min/mg) but low clearance in human microsomes ($T_{1/2}$ = 144 min, CL_{int} = 9.7 μL/min/mg). This trend continued with modest stability in mouse ($T_{1/2}$ = 82.6 min, CL_{int} = 16.8 μL/min/10^6 cells) and greater stability in human ($T_{1/2}$ = 139 min, CL_{int} = 10.0 μL/min/10^6 cells) hepatocytes. Protein plasma binding in mouse and human was 93.8% and 84.7%, respectively. Off-target effects of ***WEHI-P8*** include good selectivity (>10 μM, 7 isoforms) against 7 CYPs and low hERG binding (measured by fluorescence polarisation) (IC_{50} = 5.39 μM).

EXTENDED DATA FIGURE 7

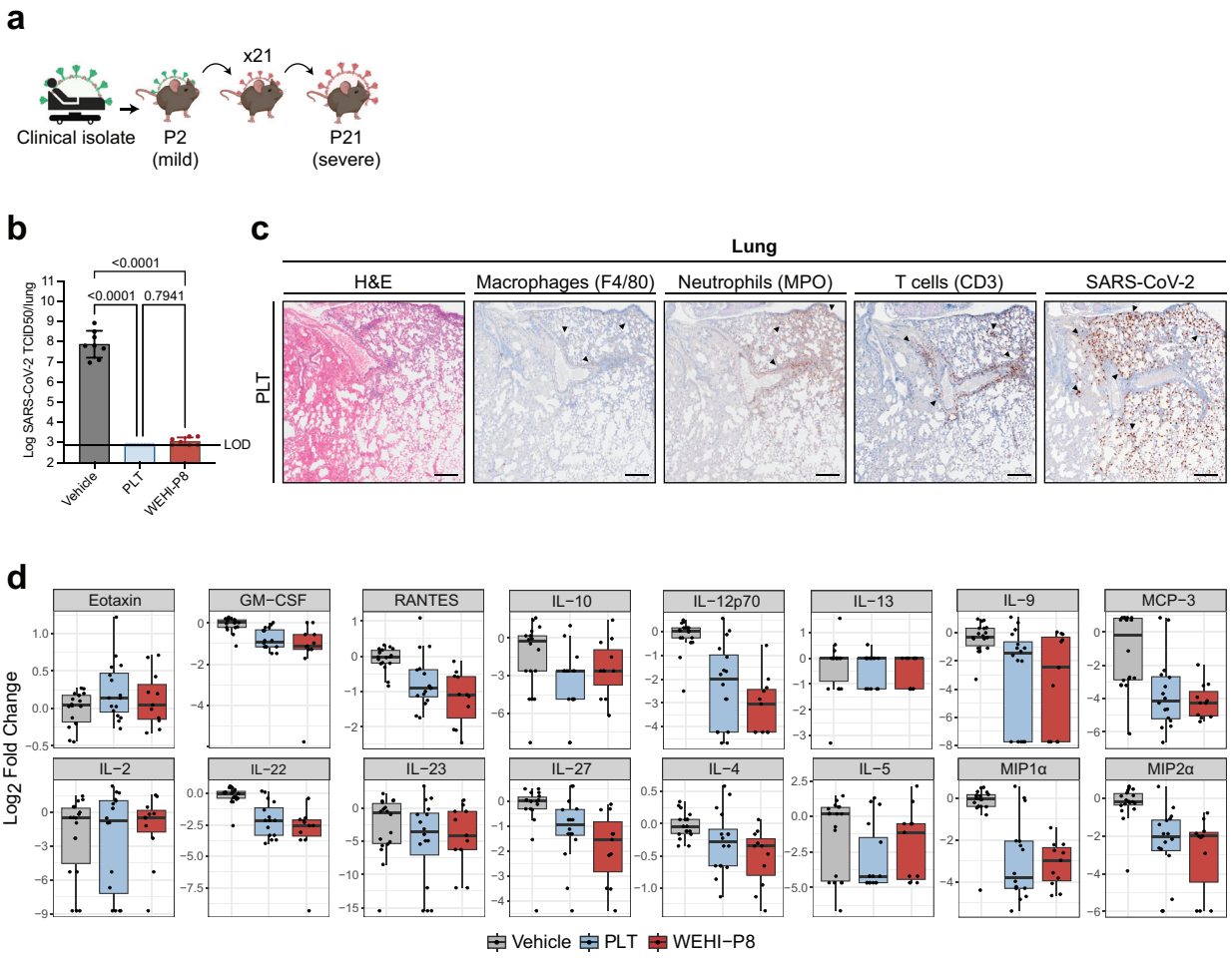

Extended Data Figure 7. Antiviral effects on acute model of mild or severe SARS-CoV-2 infection.

(a) Schematic of the serial passage method used to generate the SARS-CoV-2 strain displaying mild (P2) and severe (P21) disease (see [33] for more information). **(b)** C57BL/6 (WT) mice were infected with the SARS-CoV-2 strain P2 (mild disease) and treated with either vehicle, PLT (56 mg/kg nirmatrelvir, 19 mg/kg ritonavir), or ***WEHI-P8*** (150 mg/kg) (see schematic **Fig. 3c**). Mice were monitored for viral burden at 3 dpi (n = 7-8 mice per group, data represented as mean ± SD with p-values shown above each group). **(c)** Representative images of haematoxylin and eosin (H&E) and immunohistochemistry (IHC) stained lungs probed for F4/80 (macrophages), myeloperoxidase (MPO, neutrophils) and CD3 (T cells) are shown. Images are representative of 4 animals per group. Scale bar = 250 μm. **(d)** Levels of cytokines and chemokines measured by ELISA of lung homogenates from mice infected with severe disease (P21 strain). n = 11-18 per group; boxplots depict the median and interquartile range for each. P-values were determined by **(b)** one-way analysis of variance (ANOVA) with Tukey's multiple comparisons tests after $\log_{10}$ transformation and **(d)** Wilcoxon rank-sum test, with Bonferroni adjustment for multiple comparisons. **Source data** are available.

EXTENDED DATA FIGURE 8

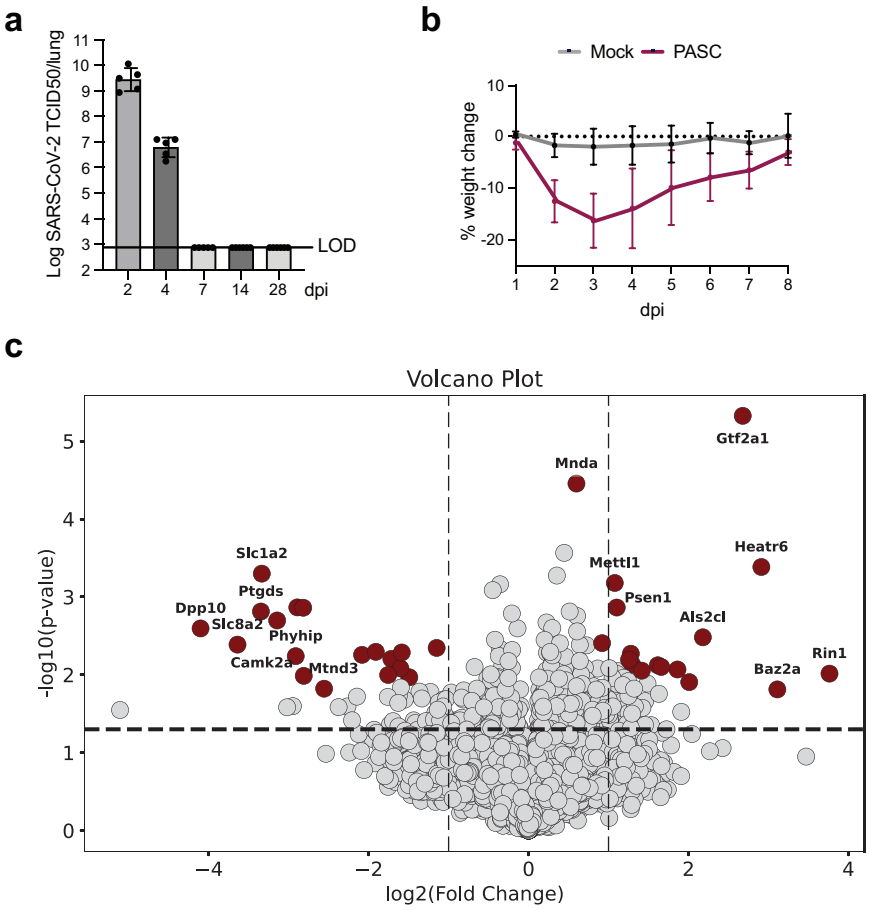

Extended Data Figure 8. Analysis of PASC mouse model.
(a) C57BL/6 (WT) mice were infected with SARS-CoV-2 P21 and monitored at different dpi for lung viral burden by TCID50 assay (n = 5 or 6 mice per time point; represented as mean ± SD). **(b)** Mice were challenged intranasally either with mock or SARS-CoV-2 P21 and monitored daily for weight loss. Animals that lost >20% of weight relative to initial weight were euthanised (results are representative of 6 independent experiments; n = 9-13 animals per group, represented as mean ± SD). **(c)** Mice were challenged intranasally with either mock or SARS-CoV-2 P21 and lungs were taken at 45 dpi for bulk proteomics analysis. Volcano plot of proteins regulated in mouse lungs 45 dpi versus mock is shown. P-values were determined by two-sided Student's t-test, false discovery rate (FDR) < 0.05 = red. **Source data** is available.

EXTENDED DATA FIGURE 9

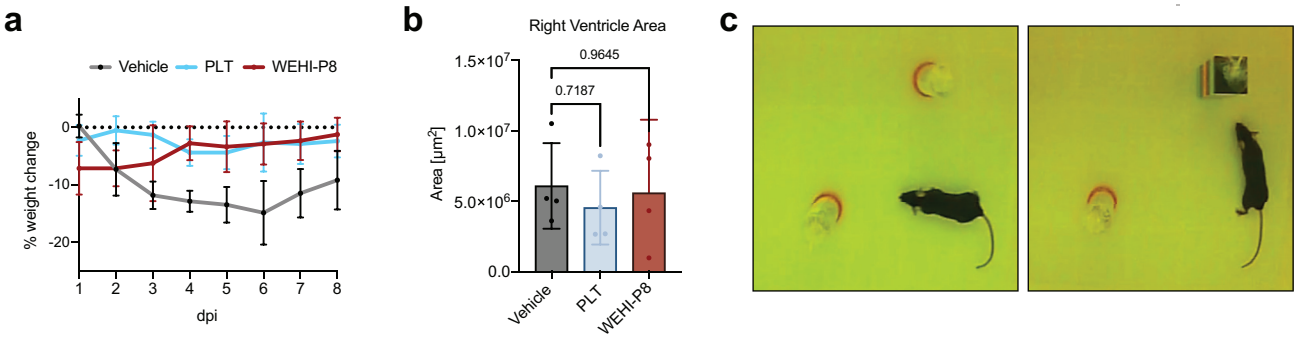

Extended Data Fig. 9. Antivirals affect PASC model

Mice were infected and treated as described in **Fig. 5a. (a)** Disease severity (as indicated by weight change) was monitored over the course of 8 dpi (results are representative of 2 independent experiments; n = 8-12 animals per group). **(b)** Hearts were collected for histological staining (H&E) and right ventricle area was quantified (n = 4 mice per group; represented as mean ± SD). P-values are shown on the respective graphs and were determined by one-way ANOVA with Tukey's multiple comparisons. **(c)** Exemplary images of novel object recognition test performed in animals after treatment and infection. Left panel: animals are introduced to a box containing two objects of the same kind. Right panel: after 1 hour break, animals are introduced to the same box, which now contains a second, novel object. Time spent exploring the familiar and novel objects is quantified. Data reported in **Fig. 5**. **Source data** is available.

EXTENDED DATA TABLE 1

	SARS-CoV-2 PLpro bound to ***WEHI-P1***	SARS-CoV-2 PLpro bound to ***WEHI-P2***	SARS-CoV-2 PLpro bound to ***WEHI-P4***	SARS-CoV-2 PLpro bound to ***WEHI-P24***
PDB ID	9CYB	9CYC	9CYD	9CYK
Data collection				
Space group	$P\ 2\ 2_1\ 2_1$	$P\ 2\ 2_1\ 2_1$	$P\ 4_3\ 3\ 2$	$P\ 2\ 2_1\ 2_1$
Cell dimensions				
a, *b*, *c* (Å)	66.46, 71.07, 176.12	66.58, 71.30, 177.51	156.59, 156.59, 156.59	67.12, 71.45, 176.45
α, β, γ (°)	90.00, 90.00, 90.00	90.00, 90.00, 90.00	90.00, 90.00, 90.00	90.00, 90.00, 90.00
Resolution (Å)	48.54 – 1.98 (2.03 – 1.98)	48.66 – 2.01 (2.06 – 2.01)	49.52 – 2.80 (2.95 – 2.80)	48.92 – 1.88 (1.92 – 1.88)
R_{merge} (within I+/I-)	0.119 (1.441)	0.066 (1.041)	0.295 (5.095)	0.062 (1.479)
Rpim (within I+/I-)	0.048 (0.580)	0.050 (0.806)	0.065 (1.129)	0.026 (0.610)
Half-Set Correlation (CC1/2)	0.999 (0.835)	0.993 (0.680)	0.999 (0.585)	1.000 (0.642)
I/σI	13.4 (1.9)	9.4 (1.1)	12.9 (1.0)	12.1 (1.1)
Completeness (%)	99.9 (98.2)	99.6 (95.7)	100 (100)	99.6 (94.9)
Redundancy	13.6 (13.6)	4.6 (4.6)	39.8 (39.9)	6.7 (6.6)
Refinement				
Resolution (Å)	37.43 – 1.98	46.93 – 2.01	49.52 – 2.80	48.92 – 1.88
No. reflections	58896	57062	16726	69303
R_{work} / R_{free}	0.181/ 0.208	0.206/ 0.237	0.241/ 0.265	0.181/ 0.212
No. atoms				
Protein	4744	4732	2450	4744
Ligand/ion	66	86	32	74
Water	253	188	0	344
B-factors				
Protein	45.1	59.0	98	48.8
Ligand/ion	36.8	61.5	69.1	42.9
Water	42.4	52.8	-	49.1
R.m.s. deviations				
Bond lengths (Å)	0.007	0.003	0.008	0.005
Bond angles (°)	0.823	0.624	0.955	0.827

*All datasets were collected from a single crystal each. *Values in parentheses are for highest-resolution shell.

1585 **Extended Data Table 1 Data Collection and Refinement Statistics.**

1586